

Electrical properties of superfilled sub-micrometer silver metallizations

D. Josell

Metallurgy Division, National Institute of Standards and Technology, Gaithersburg, Maryland 20899

C. Burkhard and Y. Li

Clarkson University, Potsdam, New York 13699

Y.-W. Cheng and R. R. Keller

Materials Reliability Division, National Institute of Standards and Technology, Boulder, Colorado 80305

C. A. Witt

Cookson Electronics-Enthone, Orange, Connecticut 06477^{a)}

D. R. Kelley, J. E. Bonevich, B. C. Baker, and T. P. Moffat

Metallurgy Division, National Institute of Standards and Technology, Gaithersburg, Maryland 20899

(Received 19 February 2004; accepted 13 April 2004)

Electrical properties of damascene silver wires with widths between ≈ 60 and 840 nm and heights between ≈ 100 nm and 300 nm are presented. The superconformal electrodeposition process by which the seam-free and void-free metallizations were fabricated is summarized. The chemical-mechanical polishing plus oblique ion sputtering process by which metal overburden was removed from the field adjacent to the wires is detailed. The size-dependent resistivity of the wires is obtained and interpreted in terms of intrinsic resistivity, grain boundary reflection, and surface scattering. Quantitative analysis of the last is accomplished using a different implementation of the Fuchs-Sondheimer formalism for wires of rectangular geometry and nonzero surface specularity that is derived herein. © 2004 American Institute of Physics. [DOI: 10.1063/1.1757655]

I. INTRODUCTION

The superconformal bottom-up filling electrodeposition process called “superfill” followed by recrystallization is now the preferred means for fabricating copper metallizations;¹ the process yields seam-free and void-free, low-resistivity interconnects. However, as dimensions are reduced below 100 nm, surface and grain boundary scatterings are beginning to undesirably impact the room-temperature electrical transmission properties of these interconnects.^{2–4} Research focused on silver metallizations (silver has a somewhat lower electrical resistivity than copper at room temperature) can become relevant if the increase of silver’s electrical resistivity with decreasing feature size is smaller than that of copper. Relevant studies include encapsulation of Ag lines,^{5–7} reactive ion etching of Ag films,⁸ etch stops and chemical-mechanical planarization of Ag,⁹ and measurements of electrical resistivity and reliability of Ag interconnects.^{6,10–12}

As with Cu, the electrical resistivity of Ag films increases significantly for thickness below 100 nm. Nonetheless, the resistivities of Cu films were still approximately twice those of corresponding silver films for thicknesses < 100 nm.¹⁰ Importantly, in all of the cited works, the Ag metallizations were fabricated by inherently subconformal physical vapor deposition. Seams or voids would be expected in wires with aspect ratio (height/width) > 0.5 fabricated by such processes.

Electrodeposition has already been used to achieve silver superfill for defect-free filling of damascene features.^{13–16} Filling of high aspect ratio, submicrometer trenches and vias was demonstrated using a commercial silver cyanide plating solution^{13,14} as well as a fully disclosed, selenocyanate catalyzed silver cyanide electrolyte.^{15,16} A significant decrease of the electrical resistivity of planar Ag deposits grown from the commercial electrolyte was observed after low-temperature annealing,¹³ a result analogous to the well-known room-temperature recrystallization of Cu electrodeposits from superfilling electrolytes. Similarly, the curvature-enhanced accelerator coverage (CEAC) model that was developed to quantify superconformal electrodeposition of copper^{17–19} also quantitatively predicted the superconformal Ag electrodeposition from both electrolytes.^{13–16}

From a process integration perspective, the present-day use of chemical vapor deposition (CVD) for fabrication of the barrier between metallization and dielectric suggests fabrication of the metal wire itself by CVD. Unfortunately, while there are numerous organometallic precursors for CVD of Ag,^{20–23} all deposition is conformal. In light of recent demonstrations of superconformal Cu CVD utilizing a surfactant catalyzed process^{24,25} (and explained using the same CEAC mechanism that explains superconformal electrodeposition processes²⁵), it is not inconceivable that superconformal Ag CVD will also be possible in the future. Lacking such a process, the silver wires for this study were made by electrodeposition using the selenocyanate catalyzed silver cyanide electrolyte, the only disclosed process that yields superfilling of trenches with relevant dimensions and aspect ratios.¹⁶

^{a)}Previously International Sematech, Austin, TX 78701.

TABLE I. Approximate dimensions of silver wires. Widths typical of the eight wire sizes (based on cross-sectioned specimens) are given for each of the three nominal wire heights; the eight wire sizes studied are enumerated from 1 to 8 going from the widest to narrowest. Values correspond to wire widths at midheight. These approximate values of width and height were used to convert resistance measurements to resistivities only where actual dimensions of the test specimens were not obtained.

Height (nm)	Wire size							
	1	2	3	4	5	6	7	8
	Widths (nm)							
100	840	330	180	150	125	100	75	50
200	840	330	160	140	120	100	80	60
300	840	340	170	140	130	110	90	75

II. EXPERIMENTAL DETAILS

A. Seed fabrication

Patterned substrates were fabricated by International Sematech (Corporate and product names are provided only for completeness of description; their inclusion does not imply NIST endorsement). Trenches in a four-point probe geometry were patterned in nominally 100 nm, 200 nm, or 300 nm thick silicon dioxide dielectric films on a silicon nitride etch-stop layer. The patterned wafers possessed neither barrier nor seed layers. Each die on the patterned wafers contained two equivalent electrical test structures for each of eight different widths. These widths ranging from as large as $\approx 0.84 \mu\text{m}$ down to as small as $\approx 0.05 \mu\text{m}$ are listed in Table I.

Electron beam evaporation was used to deposit a triseed layer containing, in sequence from the dielectric, a titanium layer, a palladium layer, and a silver layer. The base pressure for all the depositions, which were accomplished without breaking vacuum, was lower than 8×10^{-6} Pa (8×10^{-8} Torr). The pressure during the actual metal depositions did not exceed 2×10^{-5} Pa (2×10^{-7} Torr). The Ti layer was used to promote adhesion to the dielectric, while the Ag layer was the seed for the Ag electrodeposition. The Ag, with its relatively high surface mobility, dewetted when deposited directly on Ti under these vacuum conditions [Figs. 1(a)–1(c)]; the Pd provided a surface that the Ag successfully wetted [Figs. 1(d)–1(f)]. Failure to include the Pd layer resulted in beading of the Ag layer. Deposit thicknesses in the field adjacent to the features were ≈ 12 nm Ti, 15 nm Pd, and 20 nm Ag. Dimensions might have varied by as much as $\pm 10\%$ (total variation) across the specimen stage used for the seed fabrications in the eight separate batch depositions required to produce the specimens used in these studies.

The water-cooled stage on which the substrates were mounted was systematically tilted during seed fabrication in order to maximize the line-of-sight metal deposition on the sidewalls of the features. Tilt angles were dictated by consideration of shadowing in the highest aspect ratio features, and both \pm tilt angles were used. Two to three nanometers of each layer were directed straight down (i.e., 0°) to ensure coverage of the trench bottoms. A rotation axis midway between the north-south and east-west oriented trenches on the specimens yielded deposition on all sidewalls using the single tilt axis. For the deposit thicknesses and deposition

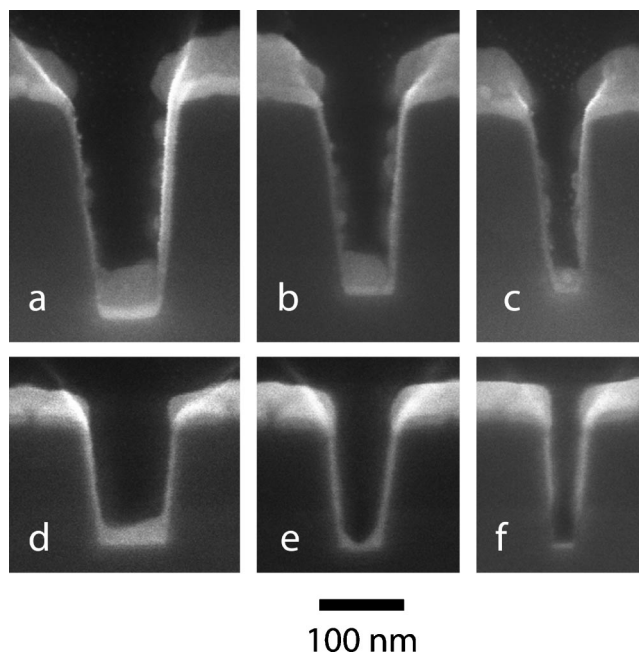


FIG. 1. Images of Ti/Ag and Ti/Pd/Ag seeds in cross-sectioned trenches. (a)–(c) In the Ti/Ag seed, the Ag on the Ti layer exhibited poor wetting in these nominally 200 nm deep trenches. (d)–(f) In the Ti/Pd/Ag seed, the Ag on the Ti/Pd layers exhibited good wetting in these nominally 100 nm deep trenches. The Ti layers are distinct in the field over the trenches as well as the trench bottoms; there is insufficient contrast to distinguish the Pd and Ag interface in (d)–(f). Sidewall shadowing during fabrication of the seeds in the lower group of images resulted in poor sidewall coverage towards the bottom of the particular highest aspect ratio feature shown in (f). The upper and lower groups of trenches are the three narrowest trenches used, sizes 6, 7, and 8 (from left to right) in the convention of Table I.

angles used, thicknesses on the sidewalls were ≈ 1 –2 nm Ti, 1–2 nm Pd, and 2–3 nm Ag, sufficient for the Ag electrodeposition.

B. Silver electrodeposition

The electrolyte was a silver cyanide solution containing 0.34 mol/L $\text{KAg}(\text{CN})_2$ and 2.3 mol/L KCN. Concentrations of KSeCN were between 20 and 50 $\mu\text{mol/L}$, consistent with previously demonstrated superconformal filling conditions.¹⁶ Depositions were conducted at room temperature ($\sim 23^\circ\text{C}$), with no agitation, at an overpotential of -0.2 V versus a Ag reference electrode. The deposition cell and procedures for assessment of electrolyte stability have been described previously.^{13–16}

C. Preparation of specimens for cross-section electron microscopy

Specimens to be cross sectioned for scanning electron microscope (SEM) imaging were covered in epoxy and a glass coverslip. They were then polished in cross section using diamond lapping films down to 1 μm grit. This was followed by directional Ar^+ polishing at 13° from the plane of the cross section, which was rotating about its normal. Because sputter removal rates of the epoxy and silver were rapid compared to those of the dielectric and Si substrate, specimens were shielded so that they only saw the Ar^+ flux

across the Si substrate. The cross-sectioned specimens were examined in a field emission scanning electron microscope.

Specimens to be studied by transmission electron microscopy (TEM) were prepared using a focused ion beam (FIB) “lift-out” technique to cut out a thin slice of the specimen that lays perpendicular to the axis of the wire of interest. This slice was placed, on its side, on a TEM specimen grid for viewing in the cross-section geometry.

D. Preparation of electrical test structures by CMP

Chemical-mechanical planarization (CMP) was used to remove most of the metal from the field over the damascene features that were destined for electrical testing. The CMP was accomplished on a LaboPol-5/LaboForce-3 polisher (Struers), a CR IC 1400-A3, 08 in., K-GRV, PSA pad (Rodel), and iCue 5001 slurry (Cabot Microelectronics), with ≈ 1 mass % H_2O_2 added as oxidizer. The polishing pressure, rotation rate (polishing platen and specimen carrier rotating independently), and slurry flow rate were 40 kPa (6 psi), 500 rpm, and 100 mL/min, respectively. Polishing times varied with deposit thickness, the Ag removal rate being ≈ 400 nm/min. Higher concentrations of H_2O_2 in the slurry induced corrosion within the features, while lower concentrations resulted in unacceptably low removal rates.

Debris was removed from the specimen surface after the CMP step by buffing in a solution of 0.5 mass % Dodecyltrimethyl-ammonium bromide (Sigma-Aldrich) surfactant in water on a Politex Reg II pad (Rodel). The polishing pressure, rotation rate, and slurry flow rate were ≈ 40 kPa, 100 rpm, and 100 mL/min, respectively.

The CMP process used did not remove the Pd and/or Ti as rapidly as the Ag. Therefore, in order to minimize removal of the damascene Ag within the filled trenches, the CMP process was halted prior to full removal of the Ag from the field, leaving both the underlying Pd and Ti layers untouched. A directional argon ion (Ar^+) flux, arriving at an angle of 7° from the plane of the specimen (which was rotating about its normal), was used to remove the remaining metal from the field around the filled trenches. Ion polishing was continued until the test structures were electrically isolated from the field as required for electrical testing. Planarization was done a minimum of one week after electrodeposition, and the specimens were stored in argon until the electrical measurement to avoid oxidation of the shallow wires.

E. Electrical measurements

Electrical-resistance measurements were conducted using a four-point probe station on the test structures. The measuring system was calibrated using NIST traceable 50 and 1000 Ω resistors (measured resistances in this study ranged between ≈ 4 and 450 Ω). The resistance was taken as the slope of current versus voltage with applied currents varying from 1 to $-1 \mu\text{A}$; ten pairs of current and voltage signals, spaced at equal current intervals, were used to obtain the slope for each resistance measurement and a minimum of three measurements were used to obtain the resistance of each test structure. At the 95% confidence level, the largest

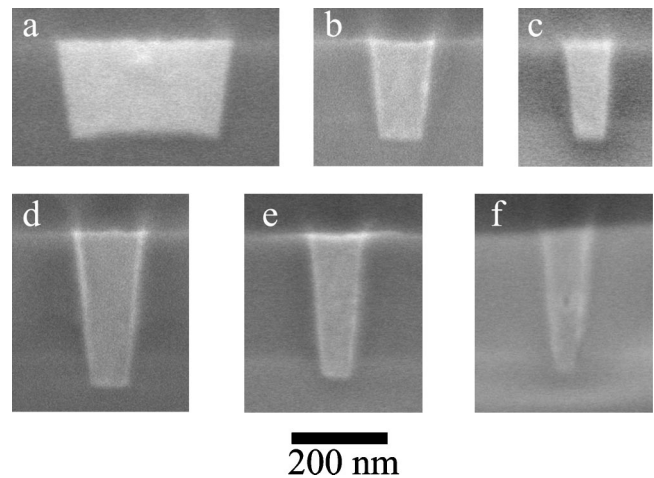


FIG. 2. SEM images of Ag damascene wires that were cross sectioned after electrical testing. The top images are of 200 nm high, intermediate width wires: (a) size 2, (b) size 5, and (c) size 7. The bottom images are of the three narrowest, 300 nm high wires: (d) size 6, (e) size 7, and (f) size 8. The void visible in (f) is typical of size 8 Ag wires of all three heights and indicates a failure to superconformally fill the narrowest wire.

uncertainty is $\pm 0.2\%$ for all measured resistance values in this study. The uncertainty decreases to less than $\pm 0.03\%$ for the narrower wires due to their larger resistances which yielded larger, and less noisy, measurement voltages.

III. EXPERIMENTAL RESULTS

A. Microstructure

With the exception of the narrowest wires (size 8, Table I), scanning electron microscopy of cross-sectioned specimens typically found no defects in the Ag wires with the Ti/Pd/Ag seed. Representative SEM images of 200 and 300 nm tall Ag wires that were cross sectioned after electrical testing are shown in Fig. 2; images of the geometry during superconformal filling have been published previously.^{13–16} Voided filling of the narrowest wires [Fig. 2(f)] was a manifestation of the limits of the superfill capability of this electrolyte; electrical data from the finest size features are included with the understanding that they are impacted by voiding. Images obtained by transmission electron microscopy are shown in Fig. 3. It is evident that these wires, with widths going well below 100 nm, filled with neither seams nor voids.

B. Feature sizes

Wire dimensions were determined from cross-sectioned specimens. Because of sidewall tilt (see Figs. 2 and 3) widths were evaluated at midheight. Typical heights and widths are given in Table I for the eight wire widths and three wire heights studied. The dimensions obtained include the areas filled by the much higher resistivity Pd and Ti seed layers (electrical resistivities of bulk Ti, Pd, and Ag are 40, 10, and 1.6 $\mu\Omega$ cm, respectively). Grain boundaries are evident in the higher aspect ratio features; only twins are visible in the lower aspect ratio features. The Ti and Pd seed is highlighted in Fig. 4. The nonuniform thickness of the bottom Ti and Pd layers results from sidewall shadowing during deposition on

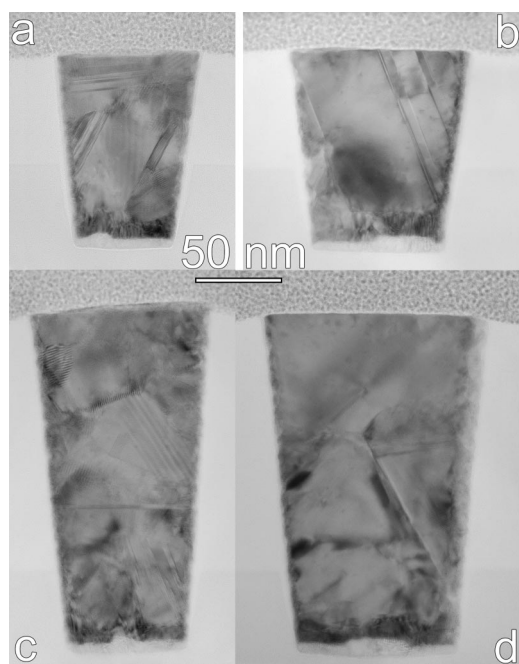


FIG. 3. Transmission electron micrographs of cross-sectioned 100 nm tall Ag wires, (a) wire 7 (≈ 75 nm wide) and (b) wire 6 (≈ 90 nm wide), and cross-sectioned 200 nm tall wires, (c) wire 6 (≈ 90 nm) and wire 5 (≈ 115 nm). The stated widths are of the pictured wires. The Ti layer is visible on the bottoms of all features as a bright region; the darker Pd layer is visible directly above the Ti layer. The bumps in the Ti and Pd layers on the bottom surface arise from overlap of the seed deposits from the \pm tilt angles. Multiple grains are evident in the higher aspect ratio wires, with grain diameter similar to the smaller dimension (width) of the wire. Only twins are visible in the wire with width similar to height.

the tilted substrate. All test structures had a $50 \mu\text{m}$ length between the voltage taps used in the four-point measurements.

C. Resistance and resistivity determination

Resistivities were obtained by multiplying the measured resistances by the appropriate wire cross-sectional areas (heights multiplied by widths) and dividing by the wire

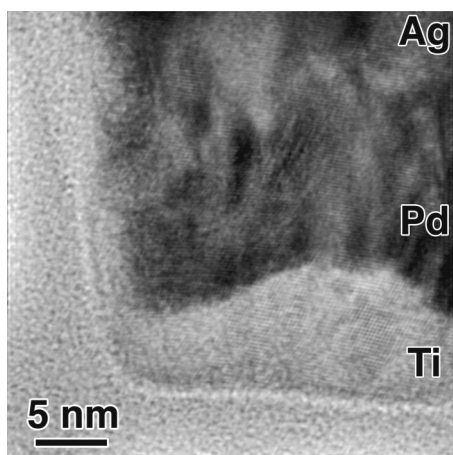


FIG. 4. Transmission electron micrograph of cross-sectioned Ag wire. Higher magnification view of the lower left corner of the Ag wire in Fig. 3(a) shows the Ti and Pd layers on the bottom of the wire.

length. The resistivities thus obtained for the 100, 200, and 300 nm tall wires are plotted versus wire width in Fig. 5. Many of the resistivity values were obtained from the measured resistances using dimensions obtained directly from the tested specimens (Fig. 5, solid symbols); the images in Figs. 3 and 4 come from a number of the cross sections prepared and examined by SEM and TEM for this purpose. Resistivities obtained using “typical” dimensions from Table I (Fig. 5, open symbols) exhibit greater scatter because of variations in cross-sectional areas. All data points exhibit scatter associated with variation in seed dimensions noted earlier.

IV. DATA ANALYSIS

A. Qualitative interpretation

The increase of the electrical resistivity with decreasing width of the Ag wires (Fig. 5) is similar to the behavior of Cu wires of similar size.² Such an effect is consistent with the feature size becoming similar to the scattering length λ (≈ 57 nm for bulk silver at room temperature). The electrical resistivity also increases as the feature height decreases. However, as will be discussed later, feature dimensions also affected the fraction of the cross section filled with the higher resistivity Ti and Pd.

B. Quantitative analysis

Quantitative understanding of the size effects in the resistivity data requires modeling scattering at both internal grain boundaries and external surfaces. Required input parameters for such modeling include feature height and width, grain size, and probabilities for specular versus diffuse scattering of electrons on the external surfaces and reflection of electrons at the internal grain boundaries. Purely diffuse surface scattering was modeled using the formalism presented in Ref. 26. The general integral equation contained therein applies to wires of all aspect ratios (and geometries). Modeling the electrical resistivity when scattering included a specular component was only slightly more complicated. Grain boundary scattering was modeled using the formalism of Ref. 27. All formulas and analyses used to interpret the experimental resistivity data are presented in the following section.

C. Modeling diffuse surface scattering

An analysis for the impact of diffuse scattering on the surfaces of a square wire on its electrical conductivity has been previously expressed in integral form.²⁸ For a wire of more general rectangular cross section, the impact of entirely diffuse surface scattering (i.e., specular scattering fraction $\epsilon = 0$) on the resistivity ρ_s of the wire, scaled by the bulk resistivity ρ_o , is obtained from Eq. (6) of Ref. 26 [or Eq. (43) of Ref. 29],

$$\frac{\rho_o}{\rho_s}(\epsilon=0, \lambda) = \frac{3}{4\pi s} \int_s ds \int_0^{2\pi} d\phi \int_0^\pi d\theta \sin\theta \cos^2\theta \times \left[1 - \exp\left(\frac{-L_{op}}{\lambda}\right) \right], \quad (1)$$

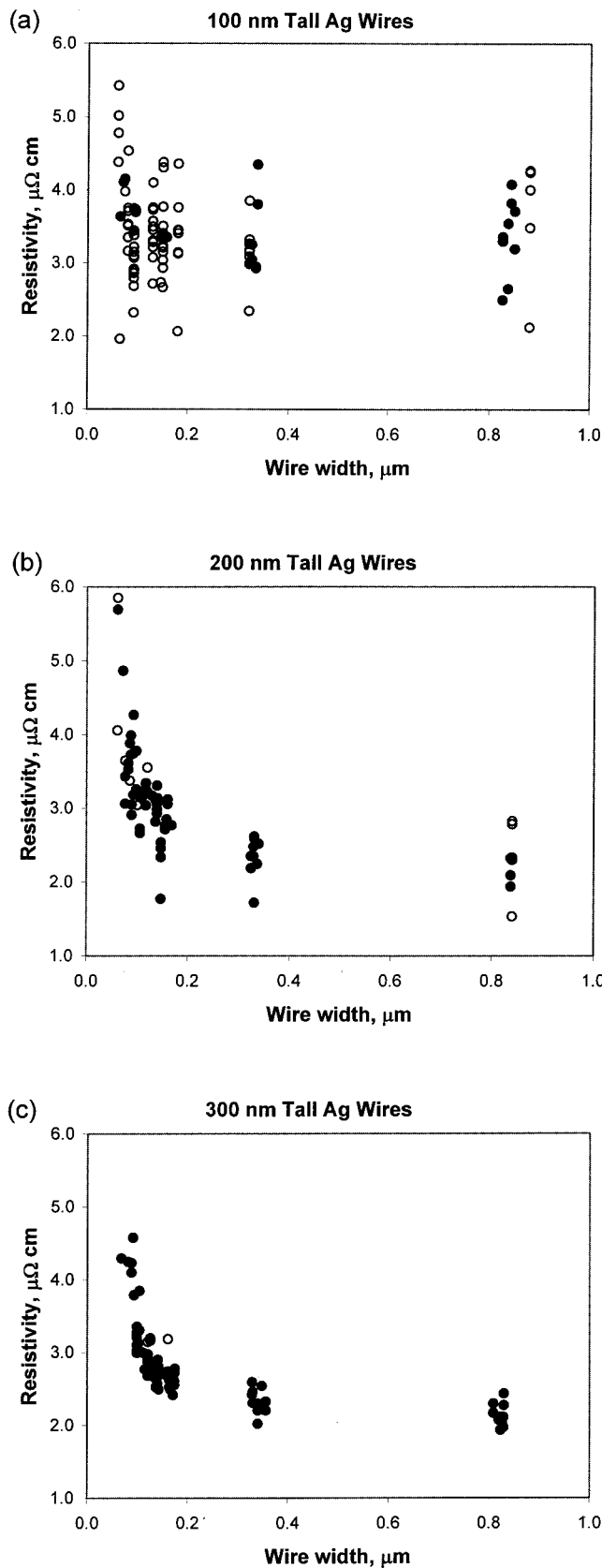


FIG. 5. (a) Resistivity data for the nominally 100 nm tall wires. (b) Resistivity data for the nominally 200 nm tall wires. (c) Resistivity data for the nominally 300 nm tall wires. All three plots show behavior vs wire width (midheight). Solid symbols are based on actual area of tested specimen. Open symbols indicate that approximate dimensions were used. In both cases, cross-sectional areas of the entire wire were used to convert measured resistances to resistivities.

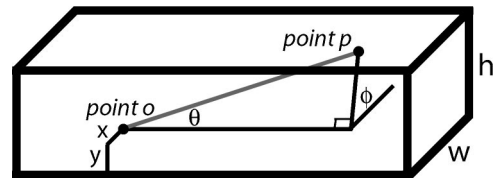


FIG. 6. The geometry under consideration in the integral for determining wire resistivity. The point o is located at coordinates x, y in the cross section. The path originating at point o and going along azimuthal angle θ and radial angle ϕ impinges on the surface of the wire at point p .

where $1 - \exp(-L_{op}/\lambda)$ is the mean free path, as a fraction of the mean free path λ in bulk material, in the presence of the diffuse scattering surface at distance L_{op} . The mean free path is reduced, because of the scattering surface, below the value λ for bulk size material with the same electron scattering properties (i.e., composition, point defect structure). The integration in Eq. (1) is over all directions from all locations in the wire cross section s , with L_{op} being the distance from the location o of the integration in the cross section to the point p on the surface of the wire in the direction at azimuthal angle θ and radial angle ϕ (see Fig. 6 for the geometry). In deriving the equations for the rectangular cross-section wire, examination of the in-plane cross section in Fig. 7 permits the following geometrical relationships to be written as

$$L_{\perp}^{1,1} = \frac{h-y}{\sin \phi},$$

$$L_{\perp}^{1,4} = \frac{-x}{\cos \phi} \tag{2}$$

for the lengths $L_{\perp}^{1,i}$ of the in-plane projections of the paths connecting point o in the cross section with p on the upper side ($L_{\perp}^{1,1}$) and left side ($L_{\perp}^{1,4}$) of the wire cross section; the choice of numbering is for convenience in the following sec-

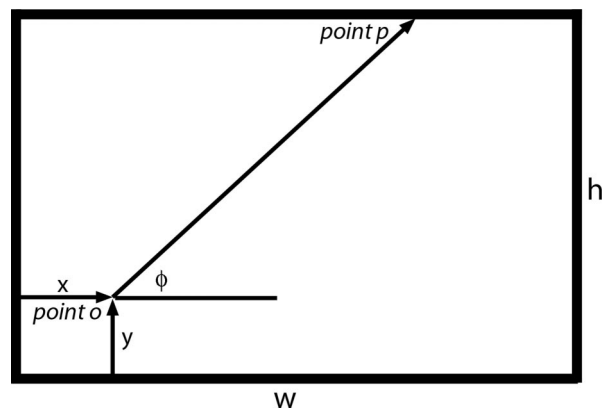


FIG. 7. The cross-section geometry of the rectangular wire. The path from point o within the cross section to the scattering point p on the surface is indicated. The radial angles ϕ defining single-segment or double-segment specular paths to the corners can be expressed in terms of the x, y coordinates of point o and the wire width w and height h . For paths at azimuthal angle θ not equal to $\pi/2$ (i.e., not perpendicular to the wire axis, see Fig. 6), the segments are understood to be in-plane projections. The radial angles thus defined apply for all values of azimuthal angle as the azimuthal angle is conserved during specular scattering on the sides of the wire.

tion. Symmetry permits consideration of only these two sides in evaluating the integral in Eq. (1) if one multiplies the integrand by a factor of 2. The length $L_{1,i}$ of the first path (between point o in the cross section to the point p on the wire surface) can be obtained directly from the in-plane projections using the spherical coordinate system to write

$$L_{1,i} = \frac{L_{\perp}^{1,i}}{\sin \theta}. \quad (3)$$

The angular ranges over which the lengths $L_{1,i}$ apply are determined from the geometry in Fig. 7,

$$\begin{aligned} \phi_0 &= \arctan\left(\frac{h-y}{w-x}\right), \\ \phi_3 &= \frac{\pi}{2} + \arctan\left(\frac{x}{h-y}\right), \\ \phi_6 &= \pi + \arctan\left(\frac{y}{x}\right) \end{aligned} \quad (4)$$

with $L_{1,1}$ applying in the range $\phi: [\phi_0, \phi_3]$, and $L_{1,4}$ applying in the range $\phi: [\phi_3, \phi_6]$. Again, the numbering scheme is chosen for convenience in the following section. The solution, with symmetry-permitted reductions of the ranges of the azimuthal and radial angles to accelerate computation for lengths and angles defined in Eqs. (2) through (4), is

$$\begin{aligned} \frac{\rho_o}{\rho_s}(\varepsilon=0, \lambda) &= \frac{3}{\pi h w} \int_0^w dx \int_0^h dy \sum_{i=0}^1 \int_{\phi_{3i}}^{\phi_{3(i+1)}} d\phi \\ &\times \int_0^{\pi/2} d\theta \sin \theta \cos^2 \theta \left[1 - \exp\left(\frac{-L_{1,3i+1}}{\lambda}\right) \right]. \end{aligned} \quad (5)$$

Though not written as such (to maintain clarity), an additional factor of 2 computational acceleration can be obtained by integrating only the first and third quadrants of the rectangular wire cross section ($0 \leq x \leq w/2$, $0 \leq y \leq h/2$, and $w/2 \leq x \leq w$, $h/2 \leq y \leq h$) and multiplying the integral by an additional factor of 2. Similar equations published to model the behavior of sub-100 nm rectangular copper wires²⁻⁴ have inadvertently included the radial, rather than azimuthal, angle in the cosine function.

D. Modeling specular scattering on surfaces

The exact solution for the resistivity when there is a nonzero specular component ε requires summing over all possible multiple scattering paths. Previous modeling for the case of nonzero specular scattering fraction ε with sub-100 nm rectangular copper wires has used the equation²⁻⁴

$$\frac{\rho_o}{\rho_s}(\varepsilon, \lambda) = (1 - \varepsilon)^2 \sum_{k=1}^{\infty} \left\{ k \varepsilon^{k-1} \left[\frac{\rho_o}{\rho_s}(\varepsilon=0, \lambda/K) \right] \right\}, \quad (6)$$

with a version of Eq. (5) in the series expansion. However, this series solution is obtained only when the specularly scattered electrons travel equal distances between successive scattering events [Eq. (9) of Ref. 26]. Thus, while Eq. (6) applies to thin film and cylindrical wire geometries, it does

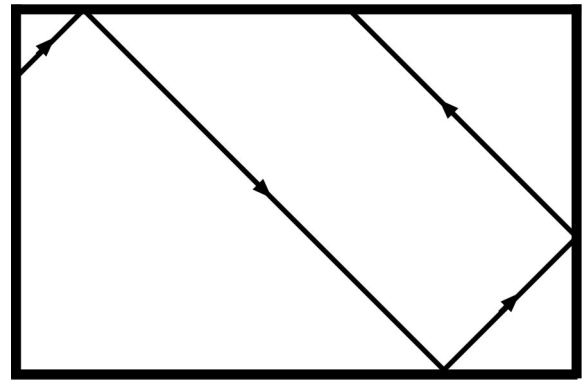


FIG. 8. Head-on view of rectangular cross-section wire showing a path with multiple specular scattering events. Note the different lengths of the (in-plane) segments.

not apply to general wire geometries. For rectangular wires in particular, the requirement of equal path lengths between successive specular scattering events is not met (Fig. 8). The use of Eq. (6) to model specular scattering in a rectangular wire is therefore an approximation. It is not possible to make a general statement concerning either the sign or size of the error associated with this approximation.

Lacking an explicit formula for this work, the exact solution for the impact of feature size on resistivity was bounded above and below as follows.

First, consistent with the exact solution, electron reflection with specular fraction ε was assumed at the first scattering site on the sidewall (point p). For the lower bound on the resistivity ρ_s , electron reflection with specular fraction ε was assumed at the second scattering site on the sidewall (point q), again consistent with the exact solution, but all subsequent scattering was neglected (underestimating the impact of surface scattering). For the upper bound, the second scattering event was modeled as entirely diffuse, $\varepsilon=0$ (overestimating the impact of surface scattering). The lower bound version of Eq. (1),

$$\begin{aligned} \frac{\rho_o}{\rho_s}(\varepsilon, \lambda) &\leq \frac{3}{4\pi s} \int_s ds \int_0^{2\pi} d\phi \int_0^{\pi} d\theta \sin \theta \cos^2 \theta \\ &\times \left[1 - (1 - \varepsilon) \exp\left(\frac{-L_{op}}{\lambda}\right) \right. \\ &\left. - \varepsilon(1 - \varepsilon) \exp\left(\frac{-(L_{op} + L_{pq})}{\lambda}\right) \right], \end{aligned} \quad (7)$$

was thus obtained by truncating the exact series solution for the resistivity to the first two scattering events [see Eq. (7) of Ref. 26 with the length definitions $L_{op} = a$ and $L_{pq} = b$]. The truncation of the series yielded the inequality sign, because all neglected terms are negative, and thus the lower bound on resistivity ρ_s . The upper bound equation

$$\frac{\rho_o}{\rho_s}(\varepsilon, \lambda) \geq \frac{3}{4\pi s} \int_s ds \int_0^{2\pi} d\phi \int_0^\pi d\theta \sin \theta \cos^2 \theta \times \left[1 - (1 - \varepsilon) \exp\left(\frac{-L_{op}}{\lambda}\right) - \varepsilon \exp\left(\frac{-(L_{op} + L_{pq})}{\lambda}\right) \right] \quad (8)$$

was obtained by replacing the $(1 - \varepsilon)$ in the last term by 1 (unity) for entirely diffuse scattering at the second site. The total uncertainty associated with the upper and lower bounds (aside from approximations implicit in the unique values of mean free path λ and specular fraction ε inherent in the Fuchs-Sondheimer formalism itself), given by the difference between Eqs. (7) and (8), is

$$\Delta \left[\frac{\rho_o}{\rho_s}(\varepsilon, \lambda) \right] = \varepsilon^2 \frac{3}{4\pi s} \int_s ds \int_0^{2\pi} d\phi \int_0^\pi d\theta \sin \theta \cos^2 \theta \times \exp\left(\frac{-(L_{op} + L_{pq})}{\lambda}\right). \quad (9)$$

The value of $(\rho_o/\rho_s)(\varepsilon, \lambda)$ that would be predicted if all multiple scattering events were included falls between the bounds obtained in Eqs. (7) and (8). The formulas for the explicit evaluation of the lower and upper bounds on the resistivity given in Eqs. (7) and (8) are derived in the Appendix.

E. Modeling reflections at grain boundaries

The modified resistivity ρ_b due to grain boundaries across the wire (i.e., a bamboo grain structure), which are spaced a distance d apart and characterized by probability R of reflecting approaching electrons, was obtained using the expression²⁷

$$\frac{\rho_o}{\rho_b} = 1 - \frac{3}{2} \alpha + 3 \alpha^2 - 3 \alpha^3 \ln\left(1 + \frac{1}{\alpha}\right),$$

where

$$\alpha \equiv \frac{\lambda}{d} \frac{R}{(1-R)}. \quad (10)$$

In modeling the experimental data, the grain size was set equal to the smaller of the wire width and height. This trend is reasonably consistent with the results of TEM examination of the fabricated wires (Fig. 3) and was previously described for sub-100 nm Cu wires.²⁻⁴

F. Model and experiment

The resistivity increase arising from the presence of both surface and grain boundary scattering was presumed to be the sum of the increases arising from the two independent effects, a standard approximation for nominally independent scattering processes. The resistivity with both scattering mechanisms being active, ρ_{sb} , is given by

$$\rho_{sb} = \rho_o + (\rho_s - \rho_o) + (\rho_b - \rho_o). \quad (11)$$

Predictions were obtained using Eq. (11), with Eq. (10) to quantify the impact of the grain boundaries and Eqs. (7) and (8), as evaluated in the Appendix, to obtain the bounds on the impact of the surface scattering.

G. Correcting for Ti and Pd seed

The wire dimensions given in Table I represent the entire metal filled cross section of each wire. However, there were ≈ 12 nm Ti and ≈ 15 nm Pd ($h_o \equiv 27$ nm) on the bottom of most of the wires. Because this region was included in the cross section for converting measured resistances to resistivities, the resistivities plotted in Fig. 5 are the effective resistivities of the entire trimetal wires. Accounting for the much higher intrinsic resistivities of the Ti and Pd regions, the resistivities of the Ag conductor itself (ρ_{Ag}) can be obtained from the experimental values plotted in Fig. 5 (ρ_{exp}) using the expression

$$\rho_{Ag} \approx \rho_{exp} \left(1 - \frac{h_o}{h}\right), \quad (12)$$

where h is the full height of the wire in nanometers. Because shadowing during deposition reduced the thicknesses of the Pd and Ti on the bottoms of the two narrowest wires (wires 7 and 8), see Figs. 1(e) and 1(f), $h_o \approx 15$ nm for correction of resistivities from wire 7 and $h_o \approx 5$ nm for correction of resistivities from wire 8. This formula yields Ag resistivities ρ_{Ag} for the nominally 300, 200, and 100 nm tall wires that are $\approx 10\%$, 13% , and 27% lower, respectively, than the plotted resistivities ρ_{exp} in Fig. 5, less for the two narrowest wires of each height.

The impact of Ti and Pd on the sidewalls (Figs. 3 and 4), ≈ 1.5 nm of each material on each side of each wire, ≈ 6 nm total, can also be included by modifying Eq. (12) to obtain

$$\rho_{Ag} \approx \rho_{exp} \left(1 - \frac{h_o}{h}\right) \left(1 - \frac{6}{w}\right), \quad (13)$$

where w is the width of the feature in nanometers. Considering just the width correction, the resistivities ρ_{Ag} of 50 nm and wider features are an additional 12% to $<1\%$ lower than the plotted resistivities ρ_{exp} in Fig. 5.

The resistivities from the 200 and 300 nm tall wires are replotted in Fig. 9 using Eq. (13) to account for the area fraction that is, essentially, nonconducting Ti or Pd. The data are plotted versus $1/\text{width}$ in order to improve visibility in the narrow widths where the resistivity is changing most rapidly. Because of the large scatter, the data from the 100 nm deep wires are not analyzed further; so they are not plotted in Fig. 9.

V. DISCUSSION

A. Fitting the data

Using a 57 nm intrinsic mean free path λ , equal to that of Ag at room temperature,³⁰ and grain spacing d , equal to the minimum of the wire height and width, predictions are overlaid on the experimental data for the 200 and 300 nm tall wires in Fig. 9. Specifically, predictions for grain boundary reflectivity $R = 0.2, 0.3,$ and 0.4 and specularity of surface

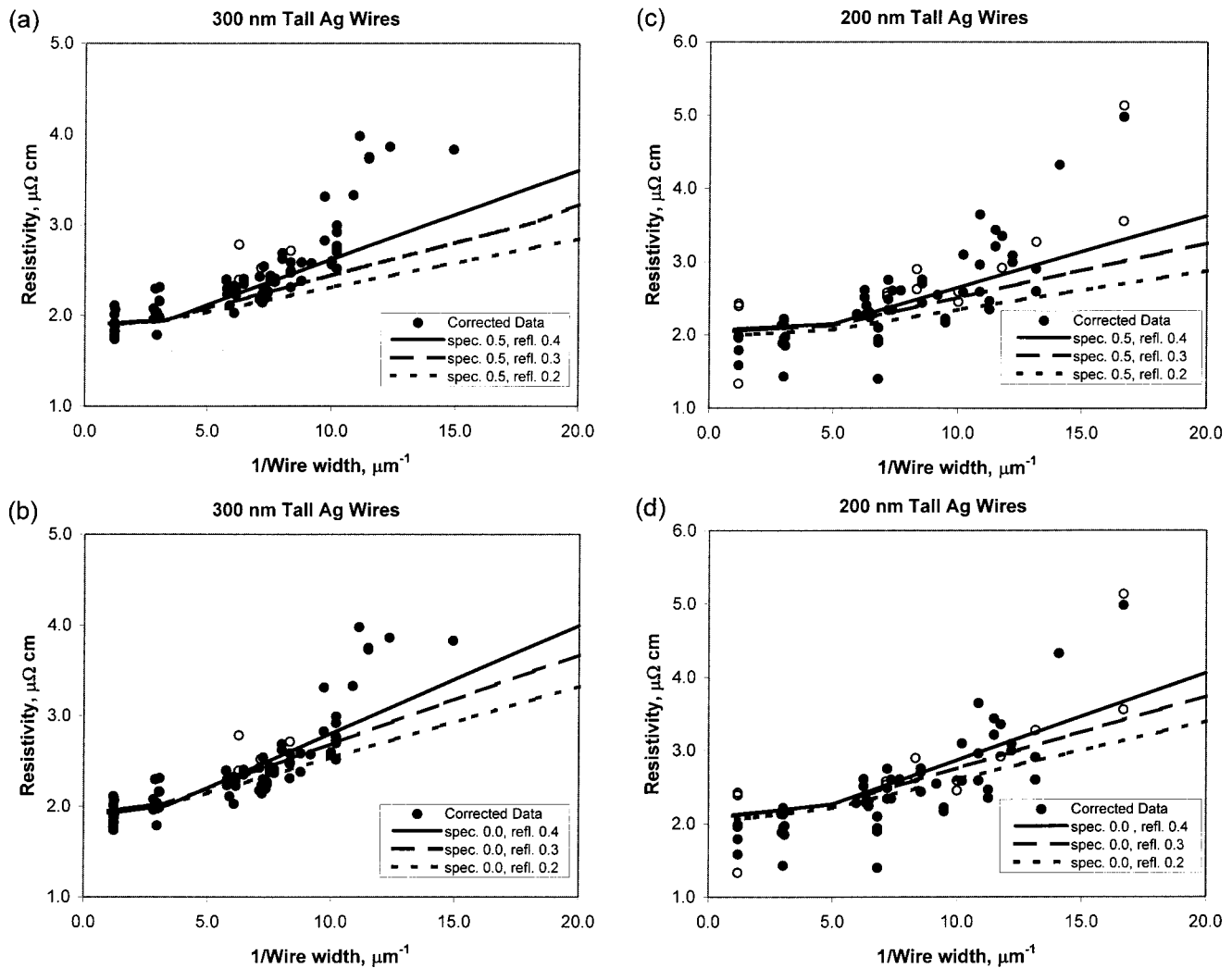


FIG. 9. (a, b) Resistivity data for the nominally 300 nm tall wires from Fig. 5(c) corrected for dimensions and nonconducting seed. (c, d) Resistivity data for the nominally 200 nm tall wires from Fig. 5(b) corrected for dimensions and nonconducting seed. All plots show behavior vs $1/\text{wire width}$ (midheight). Lower bound resistivity predictions for (a) 300 nm and (c) 200 nm tall wires with different grain boundary reflectivity and intrinsic resistivity combinations for surface specularity $\epsilon = 0.5$. Resistivity predictions for (b) 300 nm and (d) 200 nm wires with different grain boundary reflectivity and intrinsic resistivity combinations for surface specularity $\epsilon = 0.0$. Solid symbols are based on actual area of tested specimen. Open symbols indicate that approximate dimensions were used.

scattering $\epsilon = 0$ and 0.5 are given for both the 200 and 300 nm tall wires in four separate plots (a–d). In fitting the experimental data, the intrinsic resistivity ρ_0 used in the modeling was varied slightly about the $1.6 \mu\Omega$ cm value of bulk Ag in order to maintain agreement with the experimental data for the widest, tallest features; $\rho_0 = 1.65$, 1.6 , and $1.5 \mu\Omega$ cm were used with $R = 0.2$, 0.3 , and 0.4 , respectively, when $\epsilon = 0$ [Figs. 9(b) and 9(d)]. Intrinsic resistivity values were $0.05 \mu\Omega$ cm higher when $\epsilon = 0.5$ [Figs. 9(a) and 9(c)]. The possibility that ρ_0 varied with features size was not considered.

From Figs. 9(a) and 9(b), these combinations of parameters all yield the same predicted value for the size 1 (≈ 840 nm wide), 300 nm tall wire as intended. Predicted resistivities are also nearly identical for the size 1, 200 nm tall wires [Figs. 9(c) and 9(d)]. It should be pointed out that only the lower bounds [obtained from Eq. (7)] are plotted in Fig. 9 because the predictions of Eqs. (7) and (8) differ by less than 3% across the full range of widths for both the 200 and 300

nm tall wires (indicating that both the upper and lower bounds are very good approximations for the exact solution).

The predicted trend of resistivity with decreasing wire width does depend significantly on the parameters used. Specifically, the higher the value of grain boundary reflectivity the more rapid the rise of resistivity as the wire width decreases; though less obvious from the plots shown, the lower the value of specularly of surface scattering (i.e., the more diffuse), the more rapid the rise of resistivity. Both trends are to be expected. From Figs. 9(a) and 9(c), if significant specular scattering on the surfaces is assumed (i.e., $\epsilon = 0.5$), then fitting of the increase of resistivity with decreasing wire width is best with the grain boundary reflectivity $R = 0.4$ and intrinsic resistivity $\rho_0 = 1.55 \mu\Omega$ cm. On the other hand, if scattering on the surfaces is assumed to be entirely diffuse [Figs. 9(b) and 9(d) for $\epsilon = 0$], then fitting of the experimental data is better with a grain boundary reflectivity closer to 0.3 and intrinsic resistivity $1.6 \mu\Omega$ cm. The predicted contributions of the intrinsic, surface scattering, and grain bound-

TABLE II. Contributions of measured resistivity. Resistivity of 300 nm tall Ag wires over a range of widths for the case of zero surface specularity $\varepsilon = 0$, grain boundary reflectivity $R = 0.3$, and mean free path $\lambda = 57$ nm. The predicted resistivity is given along with intrinsic, surface scattering, and grain boundary reflection contributions. Grain boundary contributions are independent of width when the wires are wider than they are tall because grain size is held constant.

Wire width (μm)	Resistivity ρ_s ($\mu\Omega\text{ cm}$)	Intrinsic ($\mu\Omega\text{ cm}$)	Surface ($\mu\Omega\text{ cm}$)	Grain boundary ($\mu\Omega\text{ cm}$)
0.05	3.669	1.6	0.973	1.096
0.07	3.112	1.6	0.722	0.790
0.1	2.690	1.6	0.532	0.558
0.2	2.198	1.6	0.314	0.284
0.5	1.985	1.6	0.195	0.191
1.0	1.948	1.6	0.158	0.191

ary reflection terms to the total resistivity for 300 nm tall wires of representative widths are summarized for these parameters in Table II; a substantial grain boundary scattering contribution is associated with fitting the experimental data even though the surface scattering component is maximized by assuming entirely diffuse scattering.

The discontinuous slopes of all the predicted curves in Fig. 9, at $\approx 3 \mu\text{m}^{-1}$ in Figs. 9(a) and 9(b) and $5 \mu\text{m}^{-1}$ in Figs. 9(c) and 9(d), arise from invoking grain size equal to the minimum of wire height and width; as a result of this assumption, the grain size used in the modeling increases smoothly with wire width, until wire width equal to wire height, and then becomes constant. It is not possible to say if the data exhibit the predicted change of slope due to data scatter and the small number of wider wire sizes.

The sharp rise of resistivity at $\approx 10 \mu\text{m}^{-1}$ for the 300 nm tall wires and at $\approx 15 \mu\text{m}^{-1}$ for the 200 nm tall wires is likely associated with defects, as was noted earlier (Fig. 2). Data from these narrowest wires should therefore be viewed as an upper bound on the resistivity of Ag wires of these dimensions.

It is significant that the experimental results cannot be explained without invoking some amount of grain boundary scattering. Studies of sub-100 nm Cu wires reached a similar conclusion regarding the need to invoke some amount of grain boundary scattering to explain experimental results.²⁻⁴

B. Sources of uncertainty and error

The CMP and/or ion polishing process introduced variation of wire heights. The resulting specimen to specimen variation of wire dimensions introduced significant scatter in measured resistances for nominally identical wires. For this reason, most of the resistivity values shown were converted from the measured resistances using the dimensions of the individual tested wires (Fig. 5, closed symbols), which decreased the scatter in the evaluated resistivities significantly. Resistance data from specimens for which measured dimensions were not available were converted to resistivities using approximate dimensions from Table I (Fig. 5, open symbols). The scatter of resistivity data based on measured dimensions is the smallest for the 300 nm tall wires [Fig. 5(c)]. The scatter of the data from the 200 nm tall wires is larger [Fig.

5(b)], but still significantly smaller than that obtained using approximate dimensions. In contrast, the scatter of the resistivity data from the 100 nm tall wires did not decrease substantially when actual dimensions were used [Fig. 5(a)]. The majority of scatter in these latter data is believed to be due to uncorrected variation of the comparatively large fraction of conduction area filled with high resistivity Pd and Ti [Figs. 3(a) and 3(b)]. It was because of the comparatively poor data quality that results from the 100 nm tall specimens were not analyzed.

VI. CONCLUSION

Electrical resistivities of Ag wires from $\approx 1 \mu\text{m}$ down to below 100 nm width have been measured and analyzed. These wires were the first sub-100 nm wide Ag wires to be fabricated using a superconformal bottom-up deposition (superfill) process. Formulas for quantifying the impact of both diffuse and specular surface scattering on the resistivity of rectangular geometry wires were presented. These formulas were used, with a previously published model for grain boundary scattering, to explore the contributions of intrinsic, grain boundary, and surface scattering to the experimentally determined increase of electrical resistivity with decrease of wire dimensions. The results can be summarized as follows. The intrinsic resistivity of these Ag wires is less than $1.7 \mu\Omega\text{ cm}$, essentially the intrinsic resistivity of pure Ag. The resistivity of the Ag increases as the wire dimensions decrease toward and below 100 nm. The magnitude of the resistivity increase cannot be explained by surface scattering alone; grain boundary scattering must be invoked. The reflectivity R of the grain boundaries is most likely greater than 0.2; values higher than 0.4 require unphysical intrinsic resistivities, lower than that of pure Ag, to fit the experimental data. The data did not permit the value of the specularity ε of the wire surfaces to be determined, though it has been assumed in this paper that a value greater than 0.5 was unlikely given the complex seed geometry. Based on these results, one would expect that wires of the widths studied would exhibit substantially lower electrical resistivities if grain sizes could be increased significantly.

APPENDIX

Calculation including specular scattering

To use the general forms of Eqs. (7) and (8) with the rectangular wire geometry, the angular ranges in Eq. (4) must be subdivided to account for the three possible sides on which the second path (pq) can terminate (i.e., point q will be on a different side than point p —Fig. 8); angular subdivision for the first path (op) is the same as was used in Eq. (5). Geometry yields the following limits to the angular ranges:

$$\begin{aligned}\phi_1 &= \arctan\left(\frac{2h-y}{w-x}\right), \\ \phi_2 &= \frac{\pi}{2} + \arctan\left(\frac{x}{2h-y}\right),\end{aligned}\quad (\text{A1})$$

$$\phi_4 = \frac{\pi}{2} + \arctan\left(\frac{w+x}{h-y}\right),$$

$$\phi_5 = \pi + \arctan\left(\frac{y}{w+x}\right),$$

with ϕ_0 , ϕ_3 , and ϕ_6 already defined in Eq. (4). The in-plane (projected) lengths $L_{\perp}^{2,i}$ (between points p and q), applying over the angular ranges $\phi: [\phi_{i-1}, \phi_i]$, with $i: [1,6]$, can then be written as

$$L_{\perp}^{2,1} = \frac{w-x}{\cos \phi} - \frac{h-y}{\sin \phi},$$

$$L_{\perp}^{2,2} = \frac{h}{\sin \phi},$$

$$L_{\perp}^{2,3} = \frac{-x}{\cos \phi} - \frac{h-y}{\sin \phi},$$

$$L_{\perp}^{2,4} = \frac{h-y}{\cos(\phi - \pi/2)} - \frac{x}{\sin(\phi - \pi/2)},$$

$$L_{\perp}^{2,5} = \frac{w}{\sin(\phi - \pi/2)},$$

$$L_{\perp}^{2,6} = \frac{y}{\sin(\phi - \pi)} - \frac{x}{\cos(\phi - \pi)}.$$

As with the path from o to p , the actual length of the second path (between p and q) is its in-plane projected length divided by $\sin(\theta)$,

$$L_{2,i} = \frac{L_{\perp}^{2,i}}{\sin \theta}. \quad (\text{A3})$$

It is convenient to subdivide the two angular ranges originally defined for the op path into the same six angular ranges used for the pq path. Using Eq. (2) to define four more op path lengths

$$L_{\perp}^{1,1} = L_{\perp}^{1,2} = L_{\perp}^{1,3} = \frac{h-y}{\sin \phi},$$

$$L_{\perp}^{1,4} = L_{\perp}^{1,5} = L_{\perp}^{1,6} = \frac{-x}{\cos \phi} \quad (\text{A4})$$

permits use of the same angular ranges $\phi: [\phi_{i-1}, \phi_i]$, with $i: [1,6]$, for both the op path length $L_{\perp}^{1,i}$ and the pq path length $L_{\perp}^{2,i}$; Eqs. (3) and (A3) still define the conversion of the in-plane projections to the actual path lengths.

The integrals in Eqs. (7) and (8) can now be written explicitly for numerical evaluation:

$$\frac{\rho_o}{\rho_s}(\varepsilon, \lambda) \leq \frac{3}{\pi h w} \left\{ \int_0^w dx \int_0^h dy \sum_{i=1}^6 \int_{\phi_{i-1}}^{\phi_i} d\phi \right.$$

$$\times \int_0^{\pi/2} d\theta \sin \theta \cos^2 \theta \left[1 - (1 - \varepsilon) \exp\left(\frac{-L_{1,i}}{\lambda}\right) \right.$$

$$\left. \left. - \varepsilon (1 - \varepsilon) \exp\left(\frac{-(L_{1,i} + L_{2,i})}{\lambda}\right) \right] \right\} \quad (\text{A5})$$

and

$$\frac{\rho_o}{\rho_s}(\varepsilon, \lambda) \geq \frac{3}{\pi h w} \left\{ \int_0^w dx \int_0^h dy \sum_{i=1}^6 \int_{\phi_{i-1}}^{\phi_i} d\phi \int_0^{\pi/2} d\theta \right.$$

$$\times \sin \theta \cos^2 \theta \left[1 - (1 - \varepsilon) \exp\left(\frac{-L_{1,i}}{\lambda}\right) \right.$$

$$\left. \left. - \varepsilon \exp\left(\frac{-(L_{1,i} + L_{2,i})}{\lambda}\right) \right] \right\}, \quad (\text{A6})$$

using the definitions for ϕ_i , $L_{1,i}$, and $L_{2,i}$ given previously.

- ¹P. C. Andricacos, C. Uzoh, J. O. Dukovic, J. Horkans, and H. Deligianni, *IBM J. Res. Dev.* **42**, 567 (1998).
- ²W. Steinhögl, G. Schindler, G. Steinlesberger, and M. Engelhardt, *Phys. Rev. B* **66**, 075414 (2002).
- ³G. Schindler, W. Steinhögl, G. Steinlesberger, M. Traving, and M. Engelhardt, in *Advanced Metallization Conference 2002 Proceedings* (Materials Research Society, Pittsburgh, 2003), p. 13.
- ⁴W. Steinhögl, G. Schindler, G. Steinlesberger, M. Traving, and M. Engelhardt, in *Advanced Metallization Conference 2002 Proceedings* (Materials Research Society, Pittsburgh, 2003), p. 391.
- ⁵D. Adams and T. L. Alford, *Mater. Sci. Eng.*, **R. 40**, 207 (2003).
- ⁶T. L. Alford, P. Nguyen, Y. Zeng, and J. W. Mayer, *Microelectron. Eng.* **55**, 389 (2001).
- ⁷T. L. Alford, D. Adams, T. Laursen, and B. M. Ullrich, *Appl. Phys. Lett.* **68**, 3251 (1996).
- ⁸T. L. Alford, P. Nguyen, Y. Zeng, and J. W. Mayer, *Microelectron. Eng.* **55**, 383 (2001).
- ⁹M. Ota, M. Tsujimura, H. Inoue, H. Ezawa, and M. Miyata, *Mater. Res. Soc. Symp. Proc.* **732E**, I3.1 (2002).
- ¹⁰M. Hauder, J. Gstöttner, W. Hansch, and D. Schmitt-Landsiedel, *Appl. Phys. Lett.* **78**, 838 (2001).
- ¹¹M. Hauder, W. Hansch, J. Gstöttner, and D. Schmitt-Landsiedel, *Microelectron. Eng.* **60**, 51 (2002).
- ¹²R. Manepalli, F. Stepniak, S. A. Bidstrup-Allen, and P. A. Kohl, *IEEE Trans. Adv. Packag.* **22**, 4 (1999).
- ¹³T. P. Moffat, B. Baker, D. Wheeler, J. E. Bonevich, M. Edelstein, D. R. Kelly, L. Gan, G. R. Stafford, P. J. Chen, W. F. Egelhoff, and D. Josell, *J. Electrochem. Soc.* **149**, C423 (2002).
- ¹⁴D. Josell, B. Baker, C. Witt, D. Wheeler, and T. P. Moffat, *J. Electrochem. Soc.* **149**, C637 (2002).
- ¹⁵B. C. Baker, C. Witt, D. Wheeler, D. Josell, and T. P. Moffat, *Electrochem. Solid-State Lett.* **6**, C67 (2003).
- ¹⁶B. C. Baker, M. Freeman, B. Melnick, D. Wheeler, D. Josell, and T. P. Moffat, *J. Electrochem. Soc.* **150**, C61 (2003).
- ¹⁷D. Josell, D. Wheeler, W. H. Huber, and T. P. Moffat, *Phys. Rev. Lett.* **87**, 016102 (2001).
- ¹⁸T. P. Moffat, D. Wheeler, W. H. Huber, and D. Josell, *Electrochem. Solid-State Lett.* **4**, C26 (2001).
- ¹⁹D. Josell, D. Wheeler, W. H. Huber, J. E. Bonevich, and T. P. Moffat, *J. Electrochem. Soc.* **148**, C767 (2001).
- ²⁰Z. Yuan, N. H. Dryden, J. J. Vittal, and R. J. Puddephatt, *Chem. Mater.* **7**, 1696 (1995).
- ²¹K.-M. Chi and Y.-H. Lu, *Chem. Vap. Deposition* **7**, 117 (2001).
- ²²E. T. Eisenbraun, A. Klaver, Z. Patel, G. Nuesca, and A. E. Kaloyeros, *J. Vac. Sci. Technol. B* **19**, 585 (2001).
- ²³W. J. Evans, D. G. Giarikos, D. Josell, and J. W. Ziller, *Inorg. Chem.* **42**, 8255 (2003).
- ²⁴E. S. Hwang and J. Lee, *Electrochem. Solid-State Lett.* **3**, 138 (2000).
- ²⁵D. Josell, S. Kim, D. Wheeler, T. P. Moffat, and S. G. Pyo, *J. Electrochem. Soc.* **150**, C368 (2003).
- ²⁶R. G. Chambers, *Proc. R. Soc. London, Ser. A* **202**, 375 (1950).
- ²⁷A. F. Mayadas and M. Shatzkes, *Phys. Rev. B* **1**, 1382 (1970).
- ²⁸K. Sarginson and D. K. C. MacDonald, *Proc. R. Soc. London, Ser. A* **203**, 227 (1950).
- ²⁹E. H. Sondheimer, *Adv. Phys.* **1**, 1 (1952).
- ³⁰M. A. Omar, *Elementary Solid State Physics* (Addison-Wesley, Reading, MA, 1975), p. 145.